AMERICAN
METEOROLOGICAL
SOCIETY

Journal of the Atmospheric Sciences

EARLY ONLINE RELEASE

This is a preliminary PDF of the author-produced manuscript that has been peer-reviewed and accepted for publication. Since it is being posted so soon after acceptance, it has not yet been copyedited, formatted, or processed by AMS Publications. This preliminary version of the manuscript may be downloaded, distributed, and cited, but please be aware that there will be visual differences and possibly some content differences between this version and the final published version.

The DOI for this manuscript is doi: 10.1175/JAS-D-16-0038.1

The final published version of this manuscript will replace the preliminary version at the above DOI once it is available.

If you would like to cite this EOR in a separate work, please use the following full citation:

Rotunno, R., G. Bryan, D. Nolan, and N. Dahl, 2016: Axisymmetric Tornado Simulations at High Reynolds Number. J. Atmos. Sci. doi:10.1175/JAS-D-16-0038.1, in press.

© 2016 American Meteorological Society

LaTeX File (.tex, .sty, .cls, .bst, .bib)
Click here to download LaTeX File (.tex, .sty, .cls, .bst, .bib) tornado_revised_ams1.tex

AMERICAN METEOROLOGICAL SOCIETY 1919
PRELIMINARY ACCEPTED VERSION

Axisymmetric Tornado Simulations at High Reynolds Number

Richard Rotunno*, George H. Bryan,

National Center for Atmospheric Research, Boulder, Colorado

David S. Nolan, and Nathan A. Dahl

Rosenstiel School of Marine and Atmospheric Science, University of Miami, Miami, FL

**Corresponding author address:* Richard Rotunno, National Center for Atmospheric Research, P. O. Box 3000, Boulder, CO 80307.

E-mail: rotunno@ucar.edu

ABSTRACT

This study is the first in a series that investigates the effects of turbulence in the boundary layer of a tornado vortex. In this part, axisymmetric simulations with constant viscosity are used to explore the relationships between vortex structure, intensity, and unsteadiness as functions of diffusion (measured by a Reynolds number Re_r) and rotation (measured by a swirl ratio S_r). A deep upper-level damping zone is used to prevent upper-level disturbances from affecting the low-level vortex. The damping zone is most effective when it overlaps with the specified convective forcing, causing a reduction to the effective convective velocity scale (W_e). With this damping in place, the tornado-vortex boundary layer shows no sign of unsteadiness for a wide range of parameters, suggesting that turbulence in the tornado boundary layer is inherently a three-dimensional phenomenon. For high Re_r, the most intense vortices have maximum mean tangential winds well in excess of W_e, and maximum mean vertical velocity exceeds three times W_e. In parameter space, the most intense vortices fall along a line that follows $S_r \sim Re_r^{-1/3}$, in agreement with previous analytical predictions by Fiedler and Rotunno. These results are used to inform the design of three-dimensional, large-eddy simulations in subsequent papers.

1. Introduction

The recent review of dynamics by Rotunno (2013, R13) put heavy emphasis on the low-Reynolds-number, mostly laminar flow seen in laboratory experiments. Figure 1 illustrates the basic model: The flow at some distance from the ground (the 'outer flow') is in rotation about a vertical axis; at the lower end of the vertical axis is the 'end-wall boundary layer' over which the outer flow comes to satisfy the no-slip condition on the lower bounding surface; the reduction of centrifugal force in the boundary layer allows the radial pressure-gradient force to accelerate boundary-layer fluid toward the center whereupon it turns to the vertical and achieves the largest vertical and tangential wind speeds in the 'end-wall vortex' ; the latter transitions through a 'vortex breakdown' to a more slowly rotating, 'two-celled vortex' (downdraft at the center). Turbulent flow occurs downstream (upward) of the vortex breakdown but not in the end-wall boundary layer. As the end-wall boundary layer directly influences end-wall-vortex intensity, it is important to know the conditions under which the end-wall boundary layer may become turbulent. This paper is the first in a series aimed at understanding the nature of turbulence in the end-wall boundary-layer and how that turbulence affects vortex intensity.

According to the review in R13, the Reynolds number for laboratory experiments and numerical simulations thereof is $O(10^4)$ which is much lower than that in natural flows which may be $O(10^9)$. Fiedler and Garfield (2010) carried out axisymmetric tornado simulations for atmospherically relevant Reynolds numbers with several different turbulence parameterizations and, in each case, the parameterizations indicated small turbulence intensities in the end-wall boundary layer (see their Fig. 8). Lewellen et al. (2000) using Large Eddy Simulations (LES, which in principle attempt to simulate flow at infinite Reynolds number) found structures similar to that schematized in Fig. 1; their Fig. 5, and the analyses in their Figs. 6a, 12a and 15a, show little evidence of resolved turbulent flow in the end-wall boundary layer. Although there is parameterized subgrid-scale turbulence in LES, one must rely on its ability to represent faithfully the effects of turbulence. However, in the absence of direct turbulence measurements from real tornadoes there is no way to determine the efficacy of such parameterizations. In the sequel to this work we report on LES of tornado-like vortices with special attention to the requirements of resolving turbulence in the end-wall boundary layer. In this first part we describe the numerical setup for constant-viscosity, axisymmetric simulations, which were used to help design our LES experiments. In the course of setting up the axisymmetric simulations, we took advantage of the opportunity to explore much higher Reynolds numbers than previously achieved in such numerical simulations to investigate the possibility of axisymmetric instability of the end-wall boundary layer.

As in the numerical experiments described in R13, the present experiments are also carried out in a closed domain. Numerical simulations of tornado-like vortices in a closed domain have the advantage that boundary conditions are unambiguous and put definite constraints on the solution. On the other hand one desires the domain size to not significantly influence the simulated vortex dynamics. Thus one must use a domain large enough for artificially enhanced viscous effects to damp disturbances originating near the vortex top (which is of little physical interest) to prevent them from propagating downward and/or recirculating to the region of interest. In the course of the present investigation it became clear that simulations at higher Reynolds numbers than used previously would require even more damping for a reasonable domain size. We find the required damping to be a significant drain on the prescribed forcing that should be accounted for when estimating the Thermodynamic Speed Limit (TSL; Fiedler and Rotunno 1986) on vortex intensity. When this is taken into account the effective TSL is much lower and easily exceeded by the present simulated vortices.

For ease of comparison with atmospheric observations spatial scales will be given in dimensional terms. However the present experiments are guided by previous studies pointing to the importance of the nondimensional input parameters characterizing the imposed rotation, updraft forcing and viscous effects, namely a Swirl Ratio, S_r and the Reynolds number, Re_r. The present series of numerical experiments allow the construction of a vortex-type regime diagram in (S_r, Re_r) extending over a large range of Re_r. (The subscript r refers to use of the radial length scale of the updraft forcing in the definitions.) These experiments cover a range of Re_r that is nearly two orders of magnitude greater than in previous studies. This extended range in Re_r, together with a large number of simulations with fine increments in S_r, add further support for the theoretical relation for the optimal state, $S_r \sim Re_r^{-1/3}$ [Eq. (10) of Fiedler (2009)].

The plan of this paper is to first describe in §2 the physical problem, put it in its meteorological context and consider the necessary trade-offs involved in its numerical solution. The governing equations and simulation design are described in §3; sensitivity tests demonstrating the need for and effects of the damping layer are described in the Appendix. Examples of the numerical solutions are described in §4 and summarized in a vortex-type regime diagram for a wide range of the control parameters (S_r, Re_r). A summary is given in §5.

2. Physical problem

Figure 2 shows a schematic diagram of the physical problem following the basic design of Fiedler (1995). The entire domain rotates at the rate Ω; with non-slip, impermeable walls at the bottom and top boundaries and an impermeable free-slip wall at $r = R$. The solution for the three velocity components in the rotating reference frame and in the cylindrical coordinates (r, θ, z) is $(u, v, w) = (0, 0, 0)$ in the absence of forcing. The prescribed forcing $F(r, z)$ is placed in the vertical momentum equation as a surrogate for the buoyancy and/or dynamic-pressure-gradient forcing in a supercell thunderstorm (Klemp 1987) while the domain rotation is intended to represent the rotation of the supercell. With $F(r,z) > 0$ an in-up-out circulation is created which, in turn, transports angular momentum inwards below the forcing maximum and locally intensifies the tangential velocity v. A boundary layer forms at the bottom and top boundaries to bring the fluid into zero motion relative to the rotating domain.

The conceptual model embodied in Fig. 2 is that the in-up meridional flow brings angular momentum inwards in the lower portion of the domain in analogy to the low-level flow (below cloud base) in a rotating thunderstorm. The flow in the upper and outer portions of the domain is, however, a much poorer analogue for the complex processes occurring in a real thunderstorm as the actual up-out flow is in-cloud, subsequently exits to a stratified atmosphere and does not return to the low-level inflow during the lifetime of the thunderstorm. Hence a modeling device must be used to make sure that disturbances near the domain top Z do not make their way back to the simulated vortex (near the origin). In Fiedler (1995) the fluid viscosity was enhanced near the domain top which required resolution of a top-side boundary layer. In the present study we choose to use a linear relaxation in time (with time constant τ) of the flow back to its unforced solution above the height z_d (Fig. 2).

3. Governing equations and numerical setup

a. Governing equations

The governing equations for a constant-density, effectively incompressible fluid in the rotating domain reference frame are

$$\frac{\partial u}{\partial t} = -u\frac{\partial u}{\partial r} - w\frac{\partial u}{\partial z} - \frac{\partial \phi}{\partial r} + 2\Omega v + \frac{v^2}{r} + \nu\left(\nabla^2 u - \frac{u}{r}\right) - \alpha\frac{u}{\tau} \tag{1a}$$

$$\frac{\partial v}{\partial t} = -u\frac{\partial v}{\partial r} - w\frac{\partial v}{\partial z} - 2\Omega u - \frac{uv}{r} + \nu\left(\nabla^2 v - \frac{v}{r}\right) - \alpha\frac{v}{\tau} \tag{1b}$$

$$\frac{\partial w}{\partial t} = -u\frac{\partial w}{\partial r} - w\frac{\partial w}{\partial z} - \frac{\partial \phi}{\partial z} + F(r,z) + \nu\nabla^2 w - \alpha\frac{w}{\tau} \tag{1c}$$

$$\frac{\partial \phi}{\partial t} = -c_s^2\left[\frac{1}{r}\frac{\partial (ru)}{\partial r} + \frac{\partial w}{\partial z}\right] \tag{1d}$$

where $\phi \equiv p/\rho$, p is the pressure, ρ is the (constant) density and $c_s = 300$ m s^{-1} is the speed of sound in air. Although maximum simulated wind speeds $V_{max} \simeq 100$ m s^{-1}, the flow is effectively solenoidal (i.e. $\nabla \cdot \mathbf{u} = \mathbf{0}$) since $(V_{max}/c_s)^2 << 1$; the assumption of solenoidal $\mathbf{u}$ is used in the formulation of the diffusion terms (e.g., Batchelor 1967, p. 604).

The equations above describe the motions of a fluid that is compressible and for which density is assumed to be constant. This equation set was chosen for two main reasons. First, we are interested primarily in flow in the lowest ~ 1 km AGL for which the constant-density assumption is valid. Secondly, this set of equations allows us to use existing numerical techniques in the modeling framework used for this study, CM1 ("Cloud Model 1"), in particular the split-explicit time integration technique for compressible flows (e.g., Wicker and Skamarock 2002) as well as existing parallelization methods for distributed-memory supercomputers for three-dimensional simulations that will be reported in future papers. In addition, there are several ancillary benefits, such as a simpler equation set for analysis purposes, and a weaker upper-level response to the updraft forcing that does not need to be damped as aggressively.

The last terms on the right hand sides of (1a)-(1c) are the linear damping terms in which the coefficient $\alpha(z)$ regulates the distance over which the full damping with time constant τ is achieved. The damping function

$$\alpha(z) = \begin{cases} \frac{1}{2}\left[1-\cos\left(\pi\frac{z-z_d}{Z-z_d}\right)\right] & \text{for } z > z_d \\ 0 & \text{for } z \leq z_d\,, \end{cases} \tag{2}$$

where $0 \leq z_d \leq Z$ defines the damping layer.

Finally the updraft forcing is defined following Nolan (2005) as

$$F(r,z) = \begin{cases} F_{\max}\cos\left(\frac{\pi}{2}\chi\right) & \text{for } \chi < 1 \\ 0 & \text{for } \chi \geq 1\,, \end{cases} \tag{3}$$

where

$$\chi = \left[\frac{(z-z_b)^2}{l_z^2} + \frac{r^2}{l_r^2}\right]^{1/2} . \tag{4}$$

The forcing function $F(r,z)$ is prescribed such that the maximum F_{max} occurs at $(r,z) = (0,z_b)$ which defines the center of an elliptically shaped region (vertical and horizontal axes, l_z and l_r, respectively) over which the forcing goes to zero. The basic velocity scale W is given by the vertical integral

$$W^2 = \int_{z_b-l_z}^{z_b+l_z} 2F(0,z)dz \quad . \tag{5}$$

With (3) substituted into (5), the velocity scale

$$W = \sqrt{\frac{8F_{max}l_z}{\pi}} \quad . \tag{6}$$

The boundary conditions are $\mathbf{u} = 0$ on the upper and lower bounding surfaces while the normal velocity and stress components are zero at $r = R$.

All together there are 10 input parameters, $\Omega, W, l_r, l_z, z_b, R, Z, \nu, \tau, z_d$ and, by Buckingham's Π theorem, 8 nondimensional parameters that determine the solution. With some hindsight we choose the following:

$$\Omega l_r/W, W l_r/\nu, l_r/l_z, l_r/z_b, l_r/R, z_b/Z, z_d/z_b, \tau W/l_r. \tag{7}$$

The first parameter is a swirl ratio S_r and the second is the Reynolds number Re_r, which respectively represent system rotation and diffusive effects (the subscript 'r' signifies that we use l_r for the length scale in the swirl ratio and Reynolds number instead of Z as used in previous studies); these are the two principle solution control parameters to be varied in the present work. The third and fourth parameters characterize the geometry of the forcing and will be fixed in rough analogy to the forcing of vertical acceleration in a supercell thunderstorm. The fifth parameter measures the forcing horizontal scale against domain width and small values will be used to insure there are no significant domain-size effects. The sixth parameter measures forcing location against domain depth; ideally one would like this parameter to be small, however computational expense militates against it. Thus the seventh and eighth parameters are chosen to damp disturbances before they can reflect from the domain top and/or recirculate to the lower inflow layer.

b. Numerical-solution method

The prognostic equations (1a)-(1d) are integrated in time using a third-order Runge-Kutta scheme, using split-explicit integration for the acoustic modes following Wicker and Skamarock (2002). To improve the stability of the split-explicit time integration method, a weak three-dimensional divergence damper on the acoustic time steps is included following Skamarock and Klemp (1992).

The radial grid spacing is 5 m for $r < 1$ km, and increases gradually to 495 m between $r = 1$ km and $r = 20$ km. For most simulations, the vertical grid spacing is 5 m for $z < 1$ km, and increases gradually to 495 m between $z = 1$ km and $z = 15$ km. An exception is that most simulations with

$Re_r \geq 320,000$ were run with vertical grid spacing of 2.5 m for $z < 0.5$ km, which better resolves the shallow boundary layers for these cases. The time step varies throughout each simulation to maintain numerical stability, taking into account both advective and diffusive processes.

c. Parameter settings

The dimensional parameters settings are given in Table 1; the fixed values are chosen to conform to the physical considerations in §2 (details on the damping layer are given in the Appendix); these values thus determine six of the eight nondimensional parameters given in Table 2. The variable dimensional parameters Ω and ν are chosen to explore the range of solutions in the nondimensional parameter space (S_r, Re_r). With the fixed dimensional values of $W = 80$ m s^{-1} and $l_r = 3000$ m, we have therefore $\Omega = S_r \times 0.026$ s^{-1} and $\nu = Re_r^{-1} \times 2.4 \times 10^5$ m^2 s^{-1}.

4. Results

Figures 3-4 contain matrices in (S_r, Re_r) showing the respective maxima of the tangential and vertical velocities averaged from 5 $\times 10^4$ to 6 $\times 10^4$ s in the lowest 1 km; unless otherwise mentioned the velocities reported herein are nondimensionalized by the effective forcing value $W_e = 66$ m s^{-1} (see the Appendix). We note that the present experimental range of Re_r is much greater than in previous studies. Specifically, the highest Reynolds number, $Re_h = Wh/\nu$, where h is the height of the domain, used in Fiedler (2009) is 40,000. Estimating from $l_r/h = 1/\sqrt{10}$ from Eq. (1) of Fiedler (1998), we find that the highest $Re_r = Re_h \times l_r/h \simeq 12,800$ in Fiedler (2009). Comparison with the highest value of $Re_r = 640,000$ used here indicates a factor 50 increase in the present experiments.

Figure 5 shows the pressure minimum (nondimensionalized by W_e^2) averaged over the same time interval. Focussing first on the latter, there is a clearly an optimal combination of S_r and Re_r that produces the greatest pressure drop; these solutions are the optimal solutions that correspond to the vortex shown in Fig. 1 in which the pressure minimum occurs above the lower surface in the end-wall vortex (Church and Snow 1985). These optimal solutions tend to occur along a diagonal line in the $S_r - Re_r$ matrix; solutions below this line in the matrix are single-cell solutions while those above the line are predominantly two-celled solutions. Figure 3 indicates that the optimal solutions can exceed the TSL, while Fig. 4 shows that the vertical velocity maxima are about twice the corresponding tangential velocity maxima, consistent with the theory of Fiedler and Rotunno (1986).

Figure 6 depicts the flow (display domain indicated in Fig. 2) for several solutions that span across the optimal solutions indicated in Figs. 3-5. These solutions generally conform to the behavior expected from previous work. As reviewed in R13, the boundary-layer thickness $\delta \propto \sqrt{\nu/\Omega}$, which can be expressed as $\delta/l_r \propto 1/\sqrt{Re_r S_r}$ in the present notation; scanning Fig. 6 across (constant S_r, varying Re_r) or vertically (constant Re_r, varying S_r), generally shows this expected behavior of the vortex boundary layer. Also consistent with the theory reviewed in R13, conservation of angular momentum applied to the two-celled vortex gives $r_c v_c \propto \Omega l_r^2$ where r_c is the the radius and v_c the tangential velocity of the two-celled vortex; with $v_c \simeq W$ based on energetics, one expects therefore that $r_c/l_r \propto S_r$; this too is generally consistent with the behavior seen by scanning Fig. 6 vertically (constant Re_r, varying S_r). The optimal solution at the middle of Fig. 6 is the result of the solution finding the appropriate relation between the radius of the end-wall vortex ($\propto \delta/l_r \propto 1/\sqrt{Re_r S_r}$) and that of the two-celled vortex ($\propto S_r$), i.e., by finding the combination in $S_r - Re_r$ space where

$$S_r \propto Re_r^{-1/3} \tag{8}$$

(Fiedler 2009, his Eq. (10)). As the (S_r, Re_r) matrices are constructed on a log-log scale a power law is represented by a straight line; the line drawn Figs. 3-5 corresponds to a $-1/3$ dependence in basic agreement with (8). Note that the constant of proportionality implied in (8) is not universal and is expected to change for parameters settings different from those given in Table 2. For example, changes in domain size or upper-level damping could change the wind speeds and pressures shown in Figs. 3-5, although we expect the relation given by (8) to hold true.

In order to obtain a more-refined estimate for the $S_r = S_r(Re_r)$ that produces the optimal vortex, additional simulations were conducted holding Re_r fixed but with finer intervals of S_r than was used in Figs. 3-5. An example is shown for $Re_r = 640,000$ in Fig. 7. From a series of such figures (not shown), the minimum value of pressure was used to define the optimal vortex. Overall results are shown in shown in Fig. 8; the agreement of the data with (8) adds further confidence in this theoretical estimate.

In earlier studies, Nolan and Farrell (1999) and Nolan (2005) claimed that the optimal configuration should follow along lines of $S_r \propto Re_r^{-1}$, which would appear as a one-to-one diagonal line on Figs. 3-5. They argued that vortex structure was largely controlled by the boundary layer, which the scaling analysis in Nolan (2005) shows is controlled by $Re_V = \Omega l_r^2/\nu = S_r Re_r$. While their numerical results seemed to support this claim, their simulations were confined mostly to the range $0.02 < S_r < 0.1$ and $400 < Re_r < 1600$. In fact, some of the contours on the left (low Re_r) sides of Figs. 3-5 appear to be bending upward, suggesting some agreement in this range. The vastly higher Reynolds numbers used in the present simulations find much better agreement with the analytical predictions of Fiedler (2009) and also produce sustained wind speeds well above the convective velocity scale.

A feature of primary importance to the present work and its sequel is the effects of turbulence. The present axisymmetric model is of course incapable of simulating turbulent flow; however axisymmetric-solution unsteadiness is an indication of an axisymmetric instability that would likely lead to three-dimensional turbulence in a LES context. Figure 9 shows the standard deviation away from the time-averaged tangential velocity for three of the cases shown in Fig. 6 corresponding to the two-celled and optimal solutions (the two single-cell solutions are steady). It is clear that the vortex column is unsteady; however there is no indication of unsteadiness in the end-wall boundary layer. Further tests with a four-fold reduction of vertical grid size (not shown) confirm the latter conclusion.The axisymmetric and three-dimensional instabilities associated with vortex breakdown and the two-celled vortex have been documented in the literature [most recently by Nolan (2012)], however Fig. 9 suggests the absence of an axisymmetric instability of the end-wall vortex.

The present results suggest that turbulence in the end-wall boundary layer of actual tornadoes must originate through some combination of three-dimensional instabilities and flow separation from surface roughness elements. We expect the effects of the consequent turbulent diffusion of momentum on the end-wall boundary layer to conform qualitatively to the present case of laminar diffusion over a smooth surface. However for quantitative estimates, some other approach is required. In the following companion papers the focus will be on investigating the effects on mean vortex intensity of three-dimensional turbulence over rough surfaces in the end-wall boundary layer using LES.

5. Conclusions

The present study of axisymmetric tornado simulations has established the basic model rationale and numerical setup for our companion studies using the technique of Large Eddy Simulation (LES) in which the effects of three-dimensional turbulence can be explicitly calculated. Working within the closed-domain design of Fiedler (1995) we find for simulations with much reduced physical diffusion that an enhanced upper-level damping is generally required to prevent spurious reflections and/or recycling of disturbances from effecting the solutions in the region of physical interest. This damping, when taken into account, lowers the estimate for the Thermodynamic Speed Limit (Fiedler and Rotunno 1986, TSL) in the simulations, making the degree to which the maximum wind exceeds the TSL (Fig. 3) under the "optimal" condition (8) all the more impressive. The optimal condition (Eq.(10) of Fiedler 2009) is validated here over a range of Reynolds numbers that is almost two orders of magnitude greater than previously demonstrated.

With respect to our companion studies, the most important result is that even with Reynolds numbers $O(10^6)$ there is no indication of axisymmetric instability in the vortex boundary layer in the present solutions. The implication is that instability and turbulence in the high-Reynolds-number vortex boundary layer must arise through three-dimensional effects. Currently these effects are totally or largely parameterized even in LES type studies (Lewellen et al. 2000). The authors are unaware of any practical way to evaluate the efficacy of such parameterizations other than with an LES model capable of resolving the large eddies in the vortex boundary layer. The latter is the subject of our following companion papers.

Acknowledgments. The National Center for Atmospheric Research is sponsored by the National Science Foundation. D. Nolan and N. Dahl were supported by the NSF through grant AGS-1265899. The authors acknowledge high-performance computing support from Yellowstone (ark:/85065/d7wd3xhc), project UMIA0009, provided by NCAR's Computational and Information Systems Laboratory.

APPENDIX

The Damping Layer

As discussed in Fiedler (1995), given the necessarily finite numerical-model domain, effects of wave reflection from the upper and/or outer boundaries should be controlled through enhanced dissipation. Within the current model setup, in which grid spacing is relatively small and Reynolds number is relatively high compared to recent studies, the most convenient method to achieve this outcome was to use the linear damping terms in (3a)–(3c). After experimenting with several configurations, we decided to overlap the updraft forcing and damping layer, as illustrated in Fig. 2, which acts to draw eddies up into the damping layer. A consequence of this configuration on the effective forcing velocity is discussed below.

To demonstrate the problem with insufficient upper-level dissipation, a simulation without the upper-level damper is shown in Fig. A1(a)–(c). In this case, $Re_r = 10,000$ and $S_r = 0.01$. A low-angular-momentum "eddy" is triggered along the upper boundary by the initial updraft forcing, which then propagates along the outer boundary, and later the lower boundary. Although not shown here, there are also eddies that can propagate up the main updraft, reflect off the upper boundary, and propagate downward into the area of interest near the surface. A Hovmöller plot at 500 m ASL (Fig. A1d) shows highly unsteady behavior in this case. In contrast, when the upper-level damper is used, the aforementioned eddies do not propagate into the lower-left corner of the domain and the resulting flow is nearly steady (Fig. A1e).

With the present damping layer [or with enhanced viscosity near the upper boundary used by Fiedler (1995)] energy is removed from the flow. To get a quantitative estimate of this effect, Fig. A2 shows the dimensional vertical velocity in the $\Omega = 0$ case, both with and without the upper damping layer. In the case without the damping layer, in which the upper boundary was placed at 25 km AGL to minimize its impact on the flow, the vertical velocity reaches a peak value of 80 m s^{-1} (black curve), precisely the value calculated from (5) or (6) (Table 1). However with the upper-layer damper, and our nominal domain depth of 15 km, the peak vertical velocity $\simeq$ 66 m s^{-1} (red curve). This latter velocity is the effective driving velocity for the tornado-like vortex solutions found here. Hence solution velocities are reported herein nondimensionalized by the effective forcing velocity, $W_e = 66$ m s^{-1}.

References

Batchelor, G. K., 1967: *An Introduction to Fluid Dynamics*. Cambridge University Press.

Church, C. R., and J. T. Snow, 1985: Measurements of axial pressures in tornado-like vortices. *J. Atmos. Sci.*, **42**, 576–582.

Fiedler, B. H., 1995: On modelling tornadoes in isolation from the parent storm. *Atmos. Ocean*, **33**, 501–512.

Fiedler, B. H., 1998: Wind-speed limits in numerically simulated tornadoes with suction vortices. *Quart. J. Roy. Meteor. Soc.*, **124**, 2377–2392.

Fiedler, B. H., 2009: Suction vortices and spiral breakdown in numerical simulations of tornado-like vortices. *Atmos. Sci. Lett.*, **10**, 109–114.

Fiedler, B. H., and G. S. Garfield, 2010: Axisymmetric tornado simulations with various turbulence models. *CFD Letters*, **2**, 112–122.

Fiedler, B. H., and R. Rotunno, 1986: A theory for the maximum windspeeds in tornado-like vortices. *J. Atmos. Sci.*, **43**, 2328–2340.

Klemp, J. B., 1987: Dynamics of tornadic thunderstorms. *Ann. Rev. Fluid Mech.*, **19**, 369–402.

Lewellen, D. C., W. S. Lewellen, and J. Xia, 2000: The influence of a local swirl ratio on tornado intensification near the surface. *J. Atmos. Sci.*, **57**, 527–544.

Nolan, D. S., 2005: A new scaling for tornado-like vortices. *J. Atmos. Sci.*, **62**, 2639–2945.

Nolan, D. S., 2012: Three-dimensional instabilities in tornado-like vortices with secondary circulations. *J. Fluid Mech.*, **711**, 61–100.

Nolan, D. S., and B. F. Farrell, 1999: The structure and dynamics of tornado-like vortices. *J. Atmos. Sci.*, **56**, 2908–2936.

Pauley, R. L., and J. T. Snow, 1988: On the kinematics and dynamics of the 18 July 1986 Minneapolis tornado. *Mon. Wea. Rev.*, **116**, 2731–2736.

Rotunno, R., 2013: The fluid dynamics of tornadoes. *Ann. Rev. Fluid Mech.*, **45**, 59–84.

Skamarock, W. C., and J. B. Klemp, 1992: The stability of time-split numerical methods for the hydrostatic and the nonhydrostatic elastic equations. *Mon. Wea. Rev.*, **120**, 2109–2127.

Wicker, L. J., and W. C. Skamarock, 2002: Time splitting methods for elastic models using forward time schemes. *Mon. Wea. Rev.*, **130**, 2088–2097.

LIST OF TABLES

TABLE 1. Parameter settings for the domain shown in Fig. 2.

R	Z	z_b	l_z	l_r	z_d	τ	W	Ω	ν
20,000 m	15,000 m	8,000 m	7,000 m	3,000 m	8,000 m	100 s	80 m s^{-1}	var.	var.

TABLE 2. Nondimensional parameters based on the dimensional parameters in Table 1.

l_r/l_z	l_r/z_b	l_r/R	z_b/Z	z_d/z_b	$\tau W/l_r$	$S_r = \Omega l_r/W$	$Re_r = W l_r/\nu$
0.429	0.375	0.150	0.533	1.0	2.7	var.	var.

LIST OF FIGURES

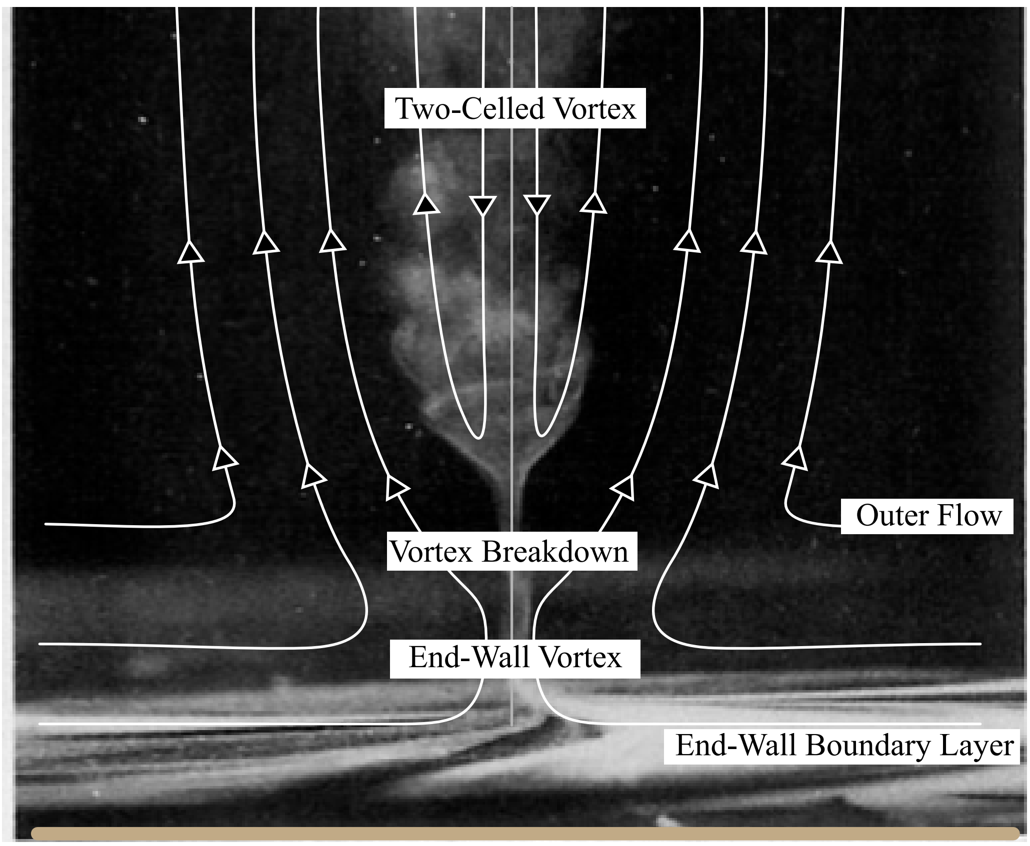

FIG. 1. A schematic diagram of the streamsurfaces in the radial-vertical plane of a laboratory vortex. The various parts of the vortex are labeled and described in the text. A photograph of a laboratory vortex (Pauley and Snow 1988) is shown in the background.

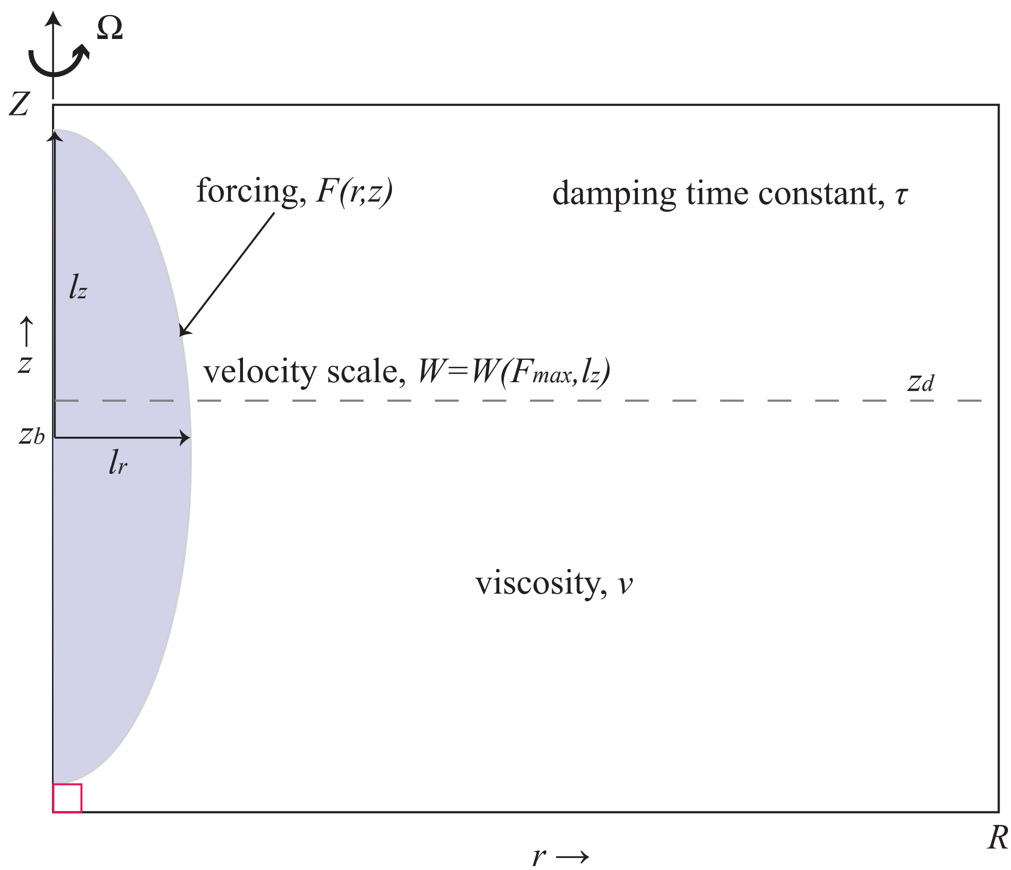

369 FIG. 2. Definition of the physical problem for the numerical simulations. Small red square is the 1 km ×1 km display domain used in Figs. 6 and 9.

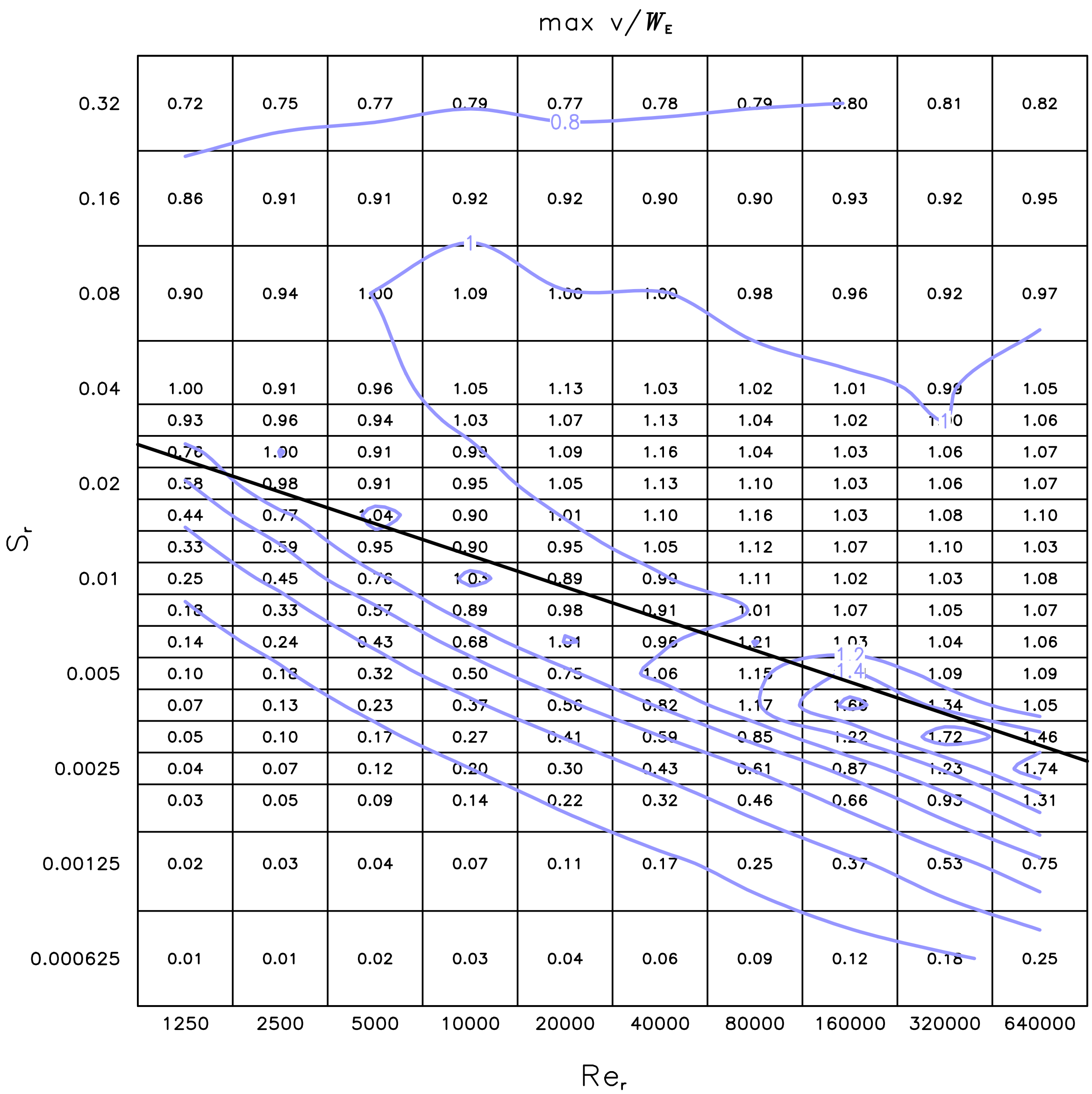

FIG. 3. Solution matrix in (S_r, Re_r) for the maximum tangential velocity divided by W_e; contour lines overlaid in intervals of 0.2. The black solid line in this and the following two figures shows $S_r \propto Re_r^{-1/3}$ dependence.

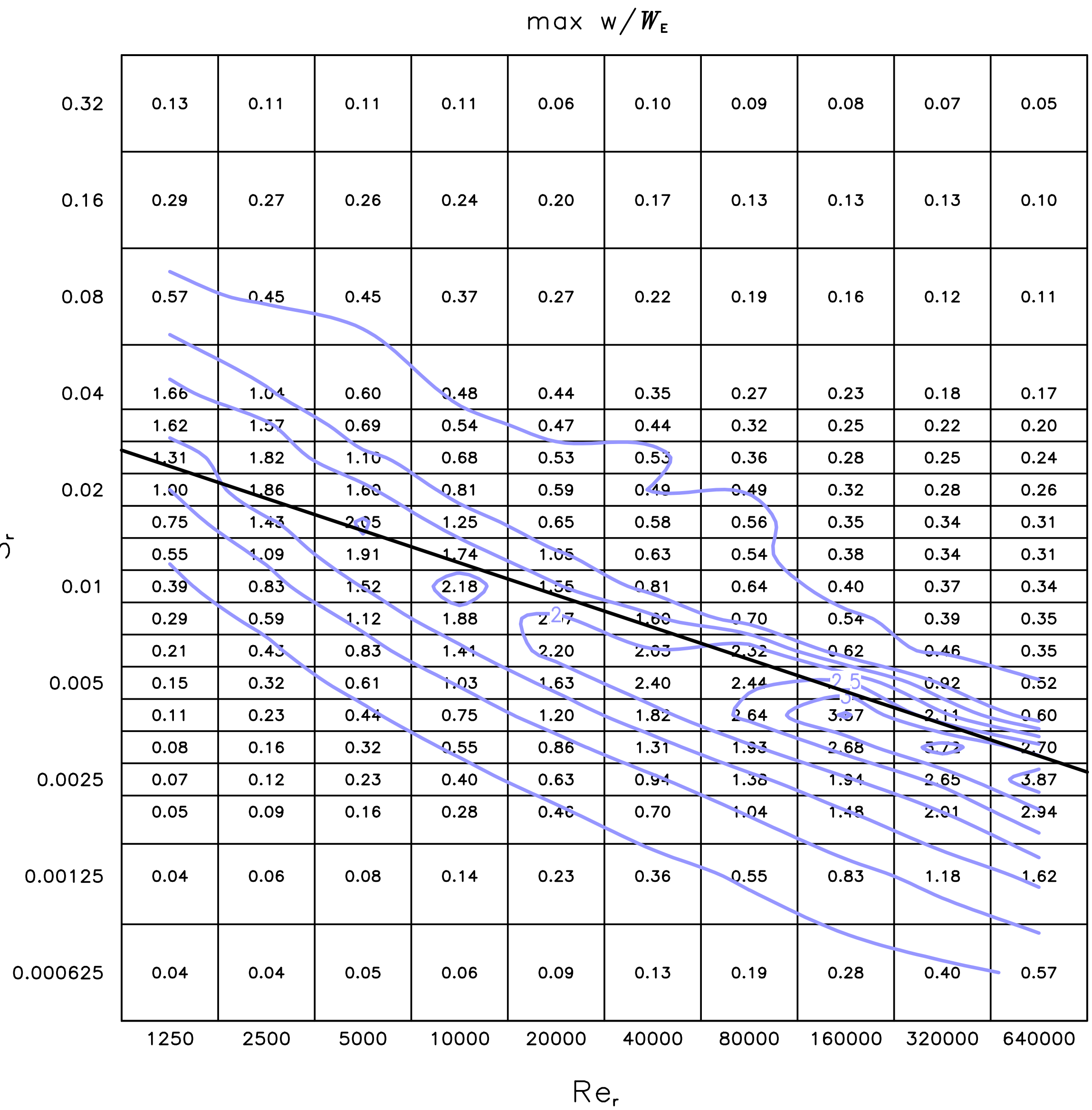

FIG. 4. Solution matrix in (S_r, Re_r) for the maximum vertical velocity divided by W_e; contour lines overlaid in intervals of 0.5.

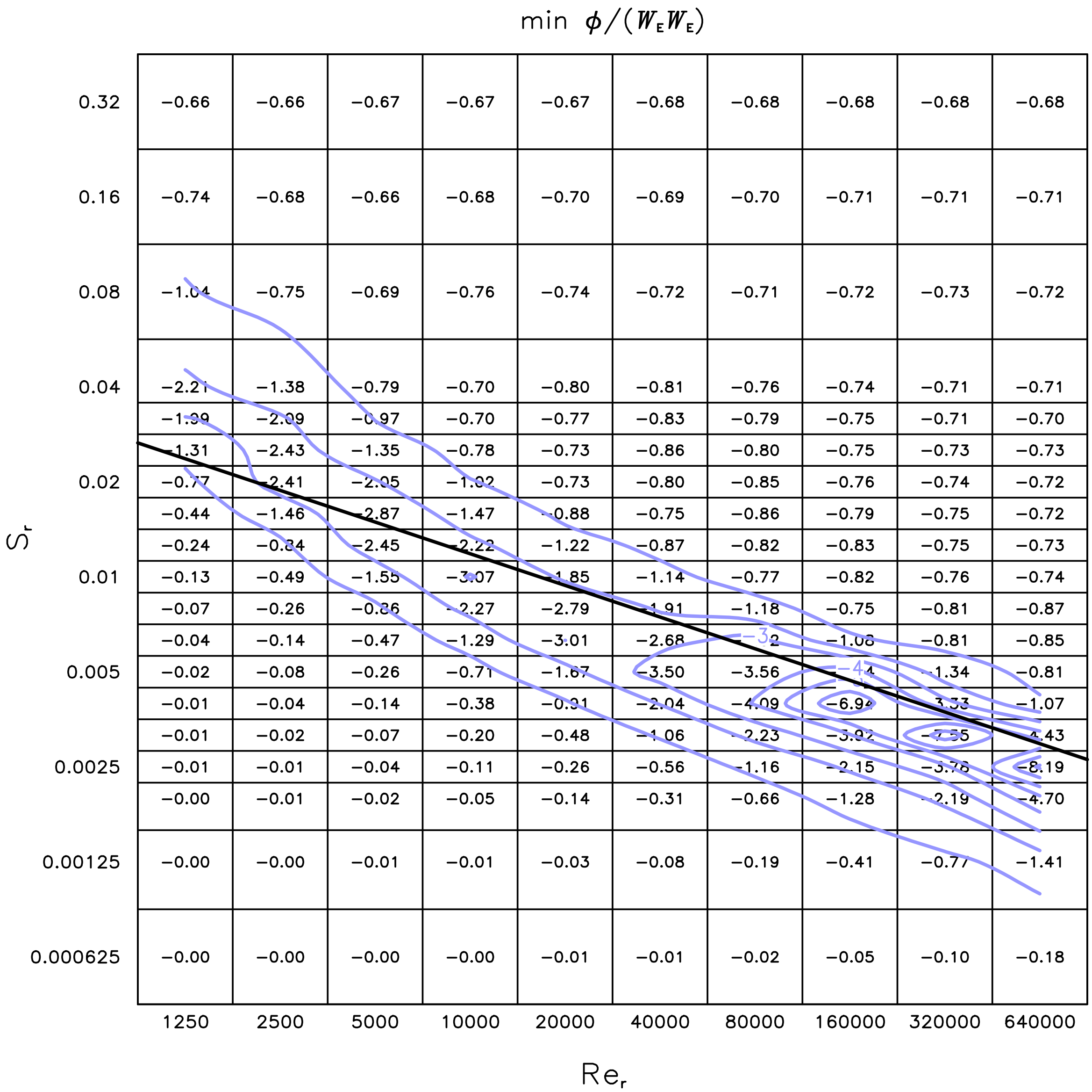

FIG. 5. Solution matrix in (S_r, Re_r) for the minimum pressure divided by W_e^2; contour lines overlaid in intervals of 1.0.

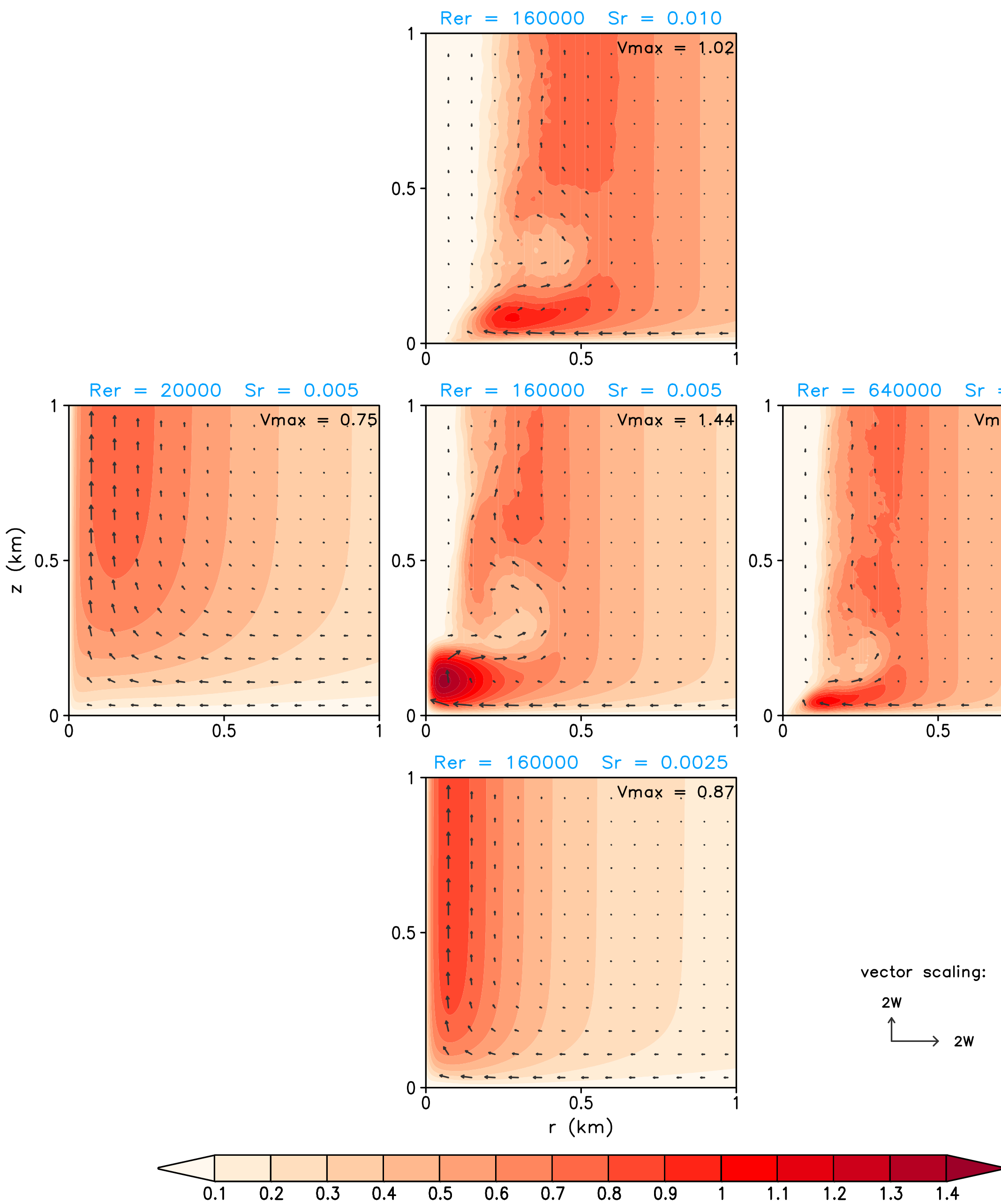

FIG. 6. Selected solutions showing the time-averaged tangential velocity divided by W_e (red shades) and radial-vertical velocity vectors. For clarity the radial velocity component has been magnified by a factor of two.

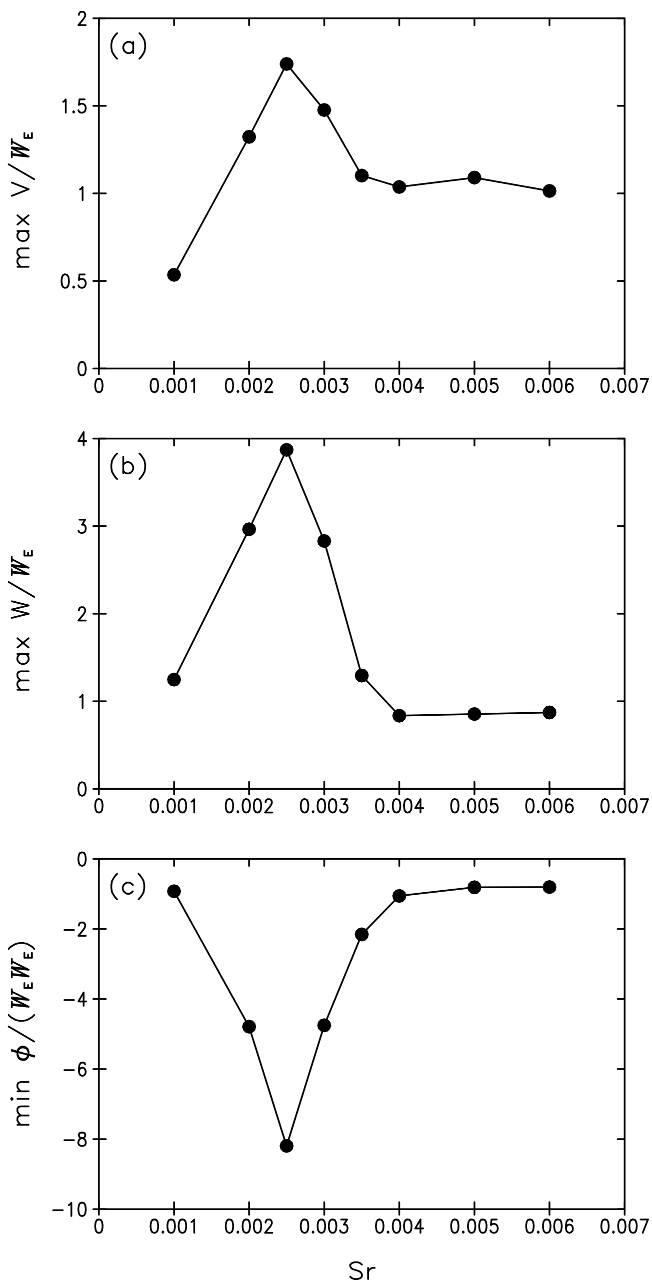

FIG. 7. Results for $Re_r = 640,000$: (a) maximum tangential velocity divided by W_e; (b) maximum vertical velocity divided by W_e; (c) minimum pressure divided by W_e^2 .

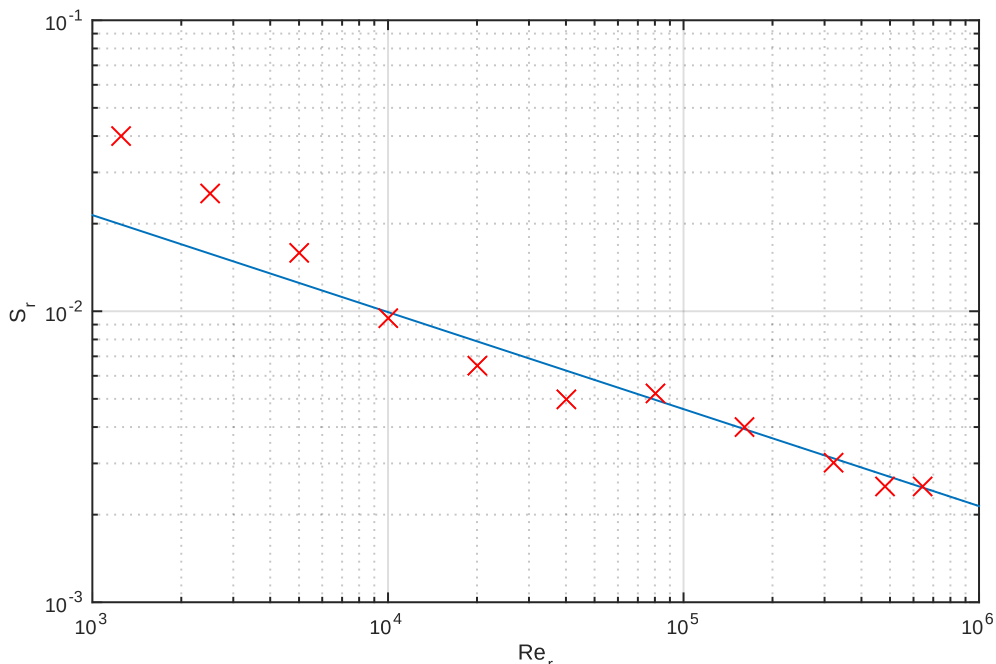

FIG. 8. A refined estimate of the validity of optimal vortex criterion (8).

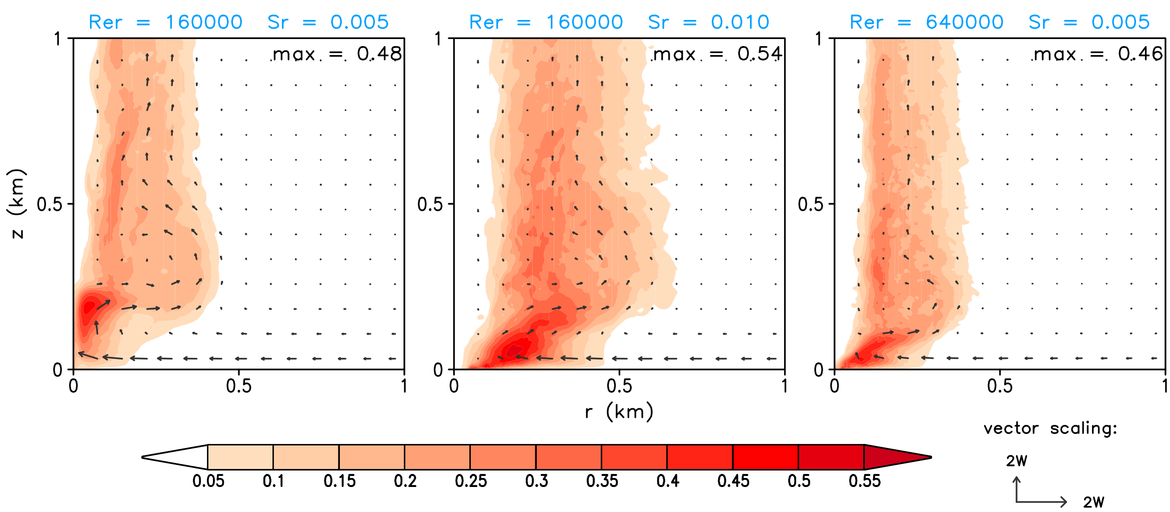

381 FIG. 9. Standard deviation of the tangential velocity divided by W_e corresponding to three of the cases shown
382 in Fig. 6. The cases with $Re_r = 160,000, S_r = 0.0025$ and $Re_r = 20,000, S_r = 0.005$ were essentially steady with
383 zero standard deviation.

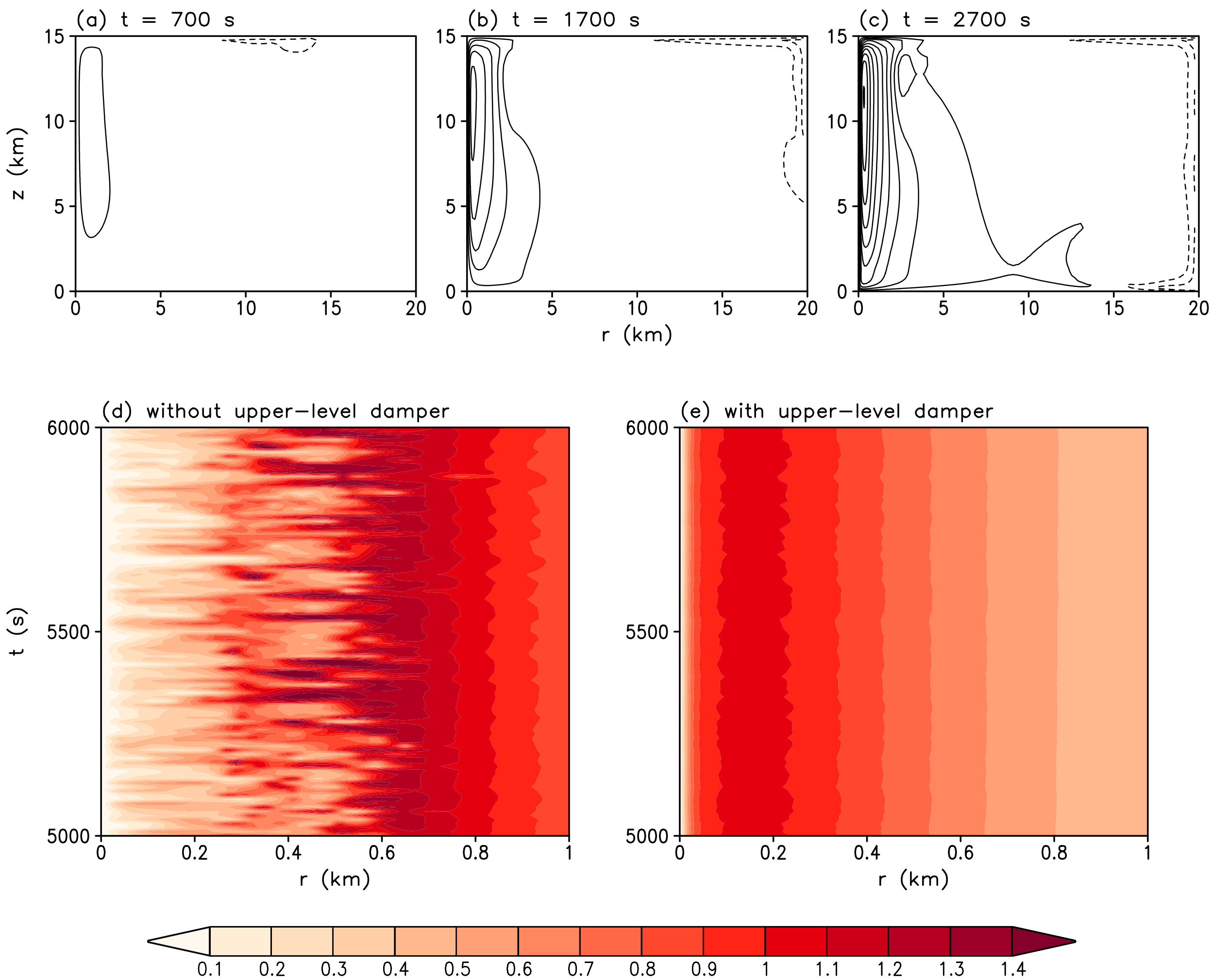

Fig. A1. Top row: tangential velocity from a simulation without upper-level damping at indicated times. The contour interval is 2 m s^{-1}, the zero contour is excluded, and negative values are dashed. Bottom row: Hovmöller diagrams of tangential velocity, normalized by W_e, at 500 m AGL from (d) a simulation without upper-level damping and (e) a simulation with upper-level damping.

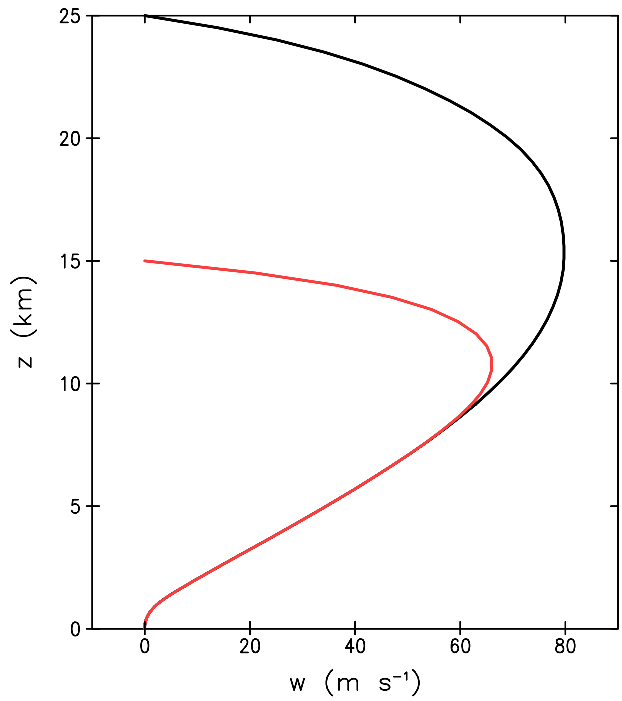

388 Fig. A2. Nonrotating solution for vertical velocity at $r = 0$ with (red curve) and without (black curve) upper-
389 layer damping.